PROCEEDINGS OF SPIE

SPIEDigitalLibrary.org/conference-proceedings-of-spie

Enhanced compressed sensing 3D SAR imaging via cross-modality EO-SAR joint-sparsity priors

Abhejit Rajagopal, Jason Hilton, David Boutte, Andrew Brown, Jan Jamora

Abhejit Rajagopal, Jason Hilton, David Boutte, Andrew P. Brown, Jan R. Jamora, "Enhanced compressed sensing 3D SAR imaging via cross-modality EO-SAR joint-sparsity priors," Proc. SPIE 12520, Algorithms for Synthetic Aperture Radar Imagery XXX, 1252003 (13 June 2023); doi: 10.1117/12.2661111

SPIE.

Event: SPIE Defense + Commercial Sensing, 2023, Orlando, Florida, United States

Enhanced Compressed Sensing 3D SAR Imaging via Cross-Modality EO-SAR Joint-Sparsity Priors

Abhejit Rajagopal[a,b], Jason Hilton[a], David Boutte[a], Andrew P. Brown[a], and Jan R. Jamora[c]

[a]Toyon Research Corporation, Goleta, California, USA 93117
[b]University of California, San Francisco, California, USA 94158
[c]Air Force Research Lab, Dayton, Ohio, USA

ABSTRACT

We introduce a compressed sensing technique for leveraging prior electro-optic (EO) imagery to improve 3D synthetic aperture radar (SAR) imaging performance. Specifically, we build on existing iterative reconstruction algorithms by guiding the reconstruction process with a joint-sparsity regularization term that captures the complementary structural information shared between EO and SAR via a sparsifying transform in the 3D image domain. We demonstrate this approach using the wavelet transform, the non-uniform Fast-Fourier transform (NUFFT), and optimizers built on autograd utilizing the 2004 AFRL Gotcha SAR dataset, with complementary EO imagery collected from the 2013 Minor Area Motion Imagery (MAMI) collection and more recent (2016) satellite collections over the same area. Results indicate significant improvements in 2D and 3D imaging performance via incorporation of the cross-modality EO prior, which we attribute to the convex problem formulation.

Keywords: synthetic aperture radar imaging, 3D reconstruction, multi-modality, compressed sensing priors

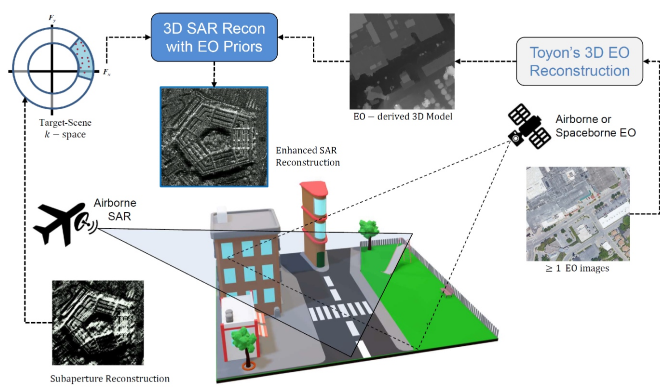

Figure 1. Our multi-modality 3D SAR imaging concept combines radar samples with concurrent *or* historical EO models via joint-sparsity regularized compressed sensing, which robustly improves imaging accuracy for narrow SAR apertures.

1. INTRODUCTION

True 3D imaging of targets is highly desirable in many intelligence, reconnaissance, and surveillance missions because it reveals geometric information about targets and target-scenes that aid in automatic target recognition, navigation, threat-level assessment, and strategic planning.[1,2] Compared to 3D reconstruction from airborne or satellite electro-optic (EO) sensors, 3D synthetic aperture radar (SAR) imaging offers the promise of enhanced target-scene characterization in all weather (day and night), from long range, and from single or limited viewing perspectives with short dwell times, enhancing the feasibility of obtaining up-to-date target-scene models in-flight.

However, 3D SAR imaging is difficult to achieve with adequate resolution in most operational settings. For example, 180° spotlight-mode aspects about an uncooperative target are infeasible to collect for platforms at range without expected target motion as in inverse SAR (ISAR).[3,4] While compressed sensing, e.g. ℓ_1-wavelet sparsity regularized reconstructions, offer dramatic improvements in image quality, these improvements are typically limited in the 2D transverse dimensions, and may not translate to enhanced 3D reconstruction performance due to a severe dearth of measurements, especially in the dimension orthogonal to the flight path and radar beam.

Distribution A: Approved for Public Release; distribution unlimited (approval number AFRL-2023-1789).

Algorithms for Synthetic Aperture Radar Imagery XXX, edited by Edmund Zelnio,
Frederick D. Garber, Proc. of SPIE Vol. 12520, 1252003 · © 2023
SPIE · 0277-786X · doi: 10.1117/12.2661111

To address this, we propose utilizing historical or concurrent EO image priors to help guide the reconstruction process. Specifically, we introduce a joint-sparsity term that seeks to capture the complementary structural information shared between EO-derived 3D models and SAR via a sparsifying transform of the 3D image domain (here we utilize `db4` Daubechies wavelets). The basic idea of our approach is to utilize the sparsity patterns of historical or concurrent EO 3D models to help guide the 3D image solution if and when they provide complementary information not captured by the data-consistency terms[5] This is an important feature of our method that makes it distinct from modality-fusion algorithms,[6,7] since our method allows utilizing 3D EO priors *even when they are not up-to-date*, without sacrificing the information content provided by the radar measurements.

2. METHODS

2.1 Problem Setup

We adopt the common monostatic radar system model:

$$y_{\text{measured}} = \mathcal{F}(\bar{K}, \bar{X}) \cdot a_{\text{true}} \tag{1}$$

where we aim to find the image $a_{\text{true}} \in \mathbb{C}^{|\bar{X}|}$ that represents the effective complex-amplitudes of $|\bar{X}|$ number of isotropic scatterers with position $\bar{X} = \{x_n \in \mathbb{R}^3\}$, using given complex-valued (IQ) radar measurements $y_{\text{measured}} \in \mathbb{C}^{|\bar{K}|\times 1}$ representing the reflection from incident radar wavevectors $\bar{K} = \{k_m \in \mathbb{R}^3\}$, with the known forward operator $\mathcal{F} : \mathbb{C}^N \to \mathbb{C}^K$ mapping complex amplitudes of the scatterers to radar data collected at the platform antenna, assumed herein to be $\mathcal{F}(k_m, x_n) = \exp(-j4\pi \cdot k_m \cdot x_n)$.

For most SAR applications, $\mathcal{F}$ is effectively rank deficient or prohibitively large, preventing direct inversion. Instead backprojection techniques attempt to invert $\mathcal{F}$ using its adjoint (i.e. $\hat{a} = \mathcal{F}^H y_{\text{measured}}$), but this relationship is only true when wavevectors in $\bar{K}$ are equispaced and ordered. Pseudo-inverse techniques can be used to yield least-square optimal solutions as $\hat{a} = \mathcal{F}^\dagger y_{\text{measured}}$, but can also prove computationally prohibitive. Instead, such minimum-norm solutions can be reformulated with gradient descent on the least-squares objective:

$$\hat{a}_{\text{least-squares}} = \underset{a}{\operatorname{argmin}} \|y_{\text{measured}} - \mathcal{F}(\bar{K}, \bar{X}) \cdot a\|_2 \tag{2}$$

This approach tends to trade memory complexity for time-complexity, which is made up for by using vectorized CPU and GPU operations. This has been used pervasively in the modern era of deep learning image reconstruction algorithms,[8,9] and can be implemented via automatic differentiation packages such as `PyTorch`, and can be combined with efficient subaperture batching approaches such as stochastic gradient descent (SGD).[10]

Unfortunately, the least-squares objective does not always yield desirable results, as seen in Figure 2.

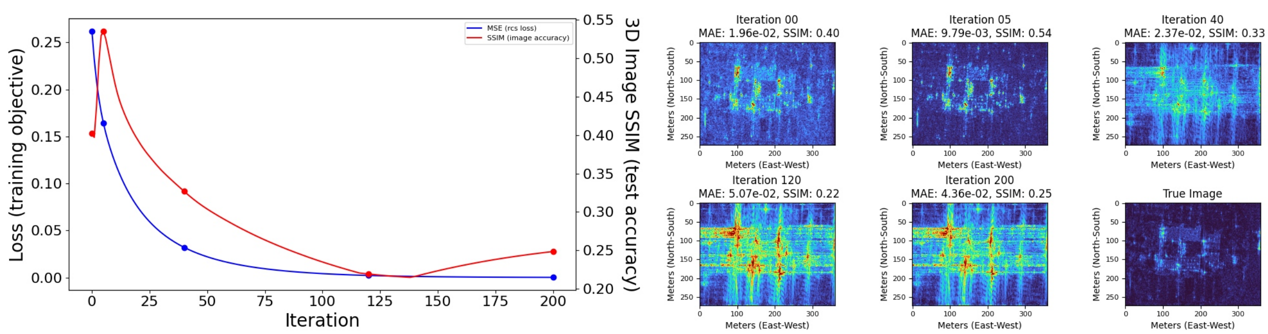

Figure 2. Optimization of the data-consistency term using mean-square error (MSE) loss and the Adam optimizer (initial learning rate 0.01). The red curve in the left plot and corresponding images on the right demonstrate that optimal image quality is not always achieved by further minimizing data-consistency (blue curve). In this example, the best image occurs around iteration number 5, with a SSIM of 0.55 with respect to the assumed groundtruth 3D SAR image.

In this vein, in this paper we show how to extend Equation 2 to compressed sensing objectives that utilize *cross-modality* EO priors to improve convergence to the solution of the ill-posed 3D inverse problem.

2.2 Datasets and Pre-processing

2.2.1 Airborne Radar Data

We utilize AFRL's GOTCHA SAR dataset, which has been described extensively in prior work.[11] Importantly, we will attempt 3D imaging using a single file composed of 6144 aperture positions with 21,232 collected frequency samples each ($\|\bar{K}\|$ =130M over 0.75° azimuth and 0.0013° elevation). Figure 3a depicts simple backprojection of the data over the entire field of view using the `FINUFFT` non-uniform Fast Fourier Transform package.[12]

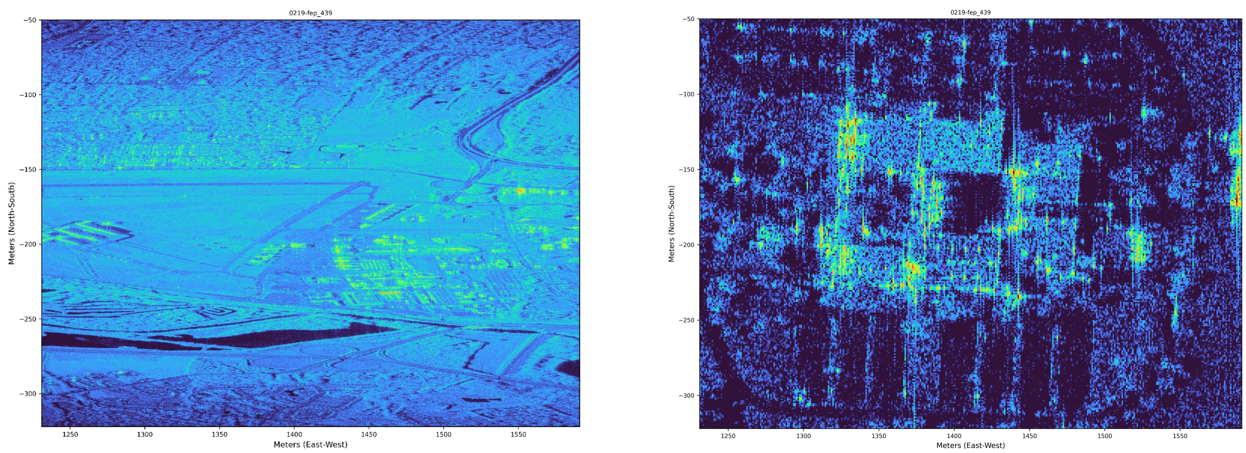

Figure 3. Backprojection of the GOTCHA data using 30K aperture points over (a) the large field of view, and (b) a small 272m × 360m ROI around the AFRL Building 620 indicated by the red box with 1m isotropic voxel spacing.

As an initial demonstration of our technique, we start by defining the ideal image a_{true} by applying a Hamming window ROI defined in Figure 3b, and subsequently generating y_{measured} by forward projecting a_{true} to the recorded antenna locations with 8000 temporal frequencies. This allows us to focus imagery over a small ROI using data-consistency terms enforcing that all the energy in the measured radar data is explained by scatterers in the target ROI. A could similarly be achieved with digital spotlighting,[13] although not used here.

In addition to radar data, we will utilize the AFRL's 2013 Minor Area Motion Imagery (MAMI) EO dataset, and more recent EO satellite collections (2016) tasked over the same area to improve image reconstruction accuracy.

2.2.2 Airborne EO Images

The first visible image dataset was a sparse sampling of 21 airborne images from AFRL's Medium Area Motion Imagery (MAMI) dataset. The images were from a wide-angle color camera and in the ROI had a GSD of approx. 0.3 m. Because our focus was on 3D reconstruction using sparse data, we sampled one image every approx. 10 seconds or every approx. 36 deg. from the MAMI video sequence. The first and last images were collected from similar perspectives during the aircraft orbit. Figure 4 shows two example images collected from approx. opposite sides of the orbit. Regions of the image outside the Air Force base had been masked out (black) by AFRL prior to data dissemination. Also note that in 8 of the images that we sampled, the buildings in the ROI were partially out-of-frame, so the number of processed images with unique perspectives and full views of the desired ROI was 12.

Our initial processing of MAMI images included camera model initialization using GPS/INS logs and camera model optimization using a dataset-specific process. A sensor orientation bias estimation and removal process was performed first, along with focal length estimation and time offset estimation (between image and GPS/INS log timestamps). Then we applied a specialized bundle adjustment process that maintains knowledge of the sensor locations while fine-tuning the sensor orientation estimates.

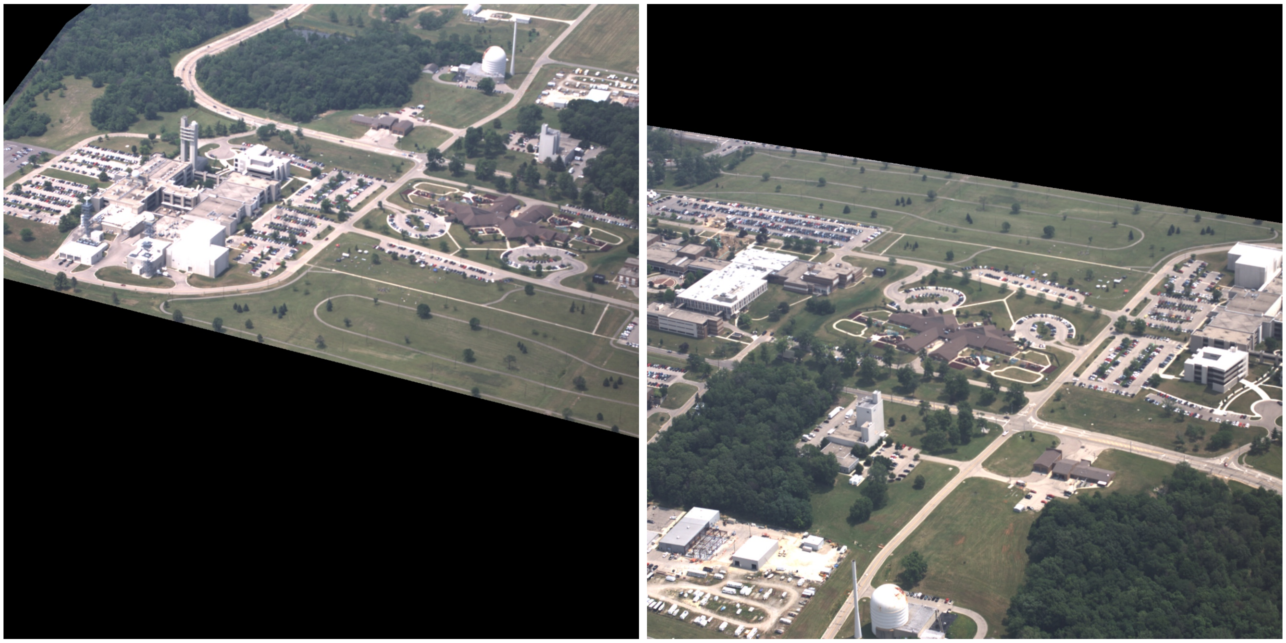

Figure 4. Two images from AFRL's MAMI data collection.

2.2.3 Stereo Satellite EO Images

The second visible image dataset was a pair of Maxar WorldView-3 satellite-based images. The processed grayscale images were collected in an in-track stereo manner with a ground sample distance (GSD) of 0.31 m. The images, cropped to the region of interest (ROI), are shown in Figure 5.

Figure 5. Pair of Maxar WorldView-3 panchromatic images cropped to the ROI.

The images and metadata were available in Basic1B format, which is closest to raw. The metadata includes an optical model as well as ephemeris tracks providing sensor 3D position and orientation (pose) information.

Since the images are collected in a pushbroom manner with each row collected at a different time, we interpolate the ephemeris to provide per-row pose estimates. We then perform image pre-processing including "undistortion" which converts the images into a form that is a good approximation for what a 2D framing sensor would collect. Jointly with this we also perform image feature extraction and association processing. Finally, we perform our bundle adjustment process which maintains sensor location estimates while finetuning sensor orientation estimates as mentioned above for the MAMI image dataset. The result is a pair of images and camera models that can be processed by our 3D reconstruction algorithm described in Section 2.2.4

2.2.4 3D EO Reconstruction

3D reconstruction processing was performed at a dense resolution with the reconstructed 3D point cloud density as fine as the input image GSD. Point cloud reconstruction was performed using a Toyon-developed Bayesian algorithm that has a number of unique features. The algorithm is designed to perform well for low-texture scenes and/or in low-SNR situations in remote sensing applications. Initial, intermediate, and final reconstruction uncertainty is characterized by the algorithm. In contrast with many top-performing reconstruction algorithms that use energy minimization and somewhat ad-hoc surface smoothness constraints, our algorithm models surface smoothness probabilistically based on the available input data and the current uncertainty distributions within an iterative reconstruction process. The algorithm also accounts for occlusion effects and applies uniqueness constraints within a probabilistic framework. The resulting dense point cloud is typically further processed to reconstruct a digital surface model (DSM).

The resulting DSMs for the satellite-based stereo and sparse MAMI images are shown in Figure 6. Each DSM has a uniform spacing of 3D points in East and North and single altitude estimate in each resolution cell. The altitudes are color-coded with yellow being lowest altitude and red being highest altitude. Example altitudes are annotated in the DSM in (b). The DSM in (b) was reconstructed in an ovular area surrounding the region of interest since image overlap tended to decrease farther from the center of the ROI. The satellite-based stereo image pair processing (a) resulted in a significantly better 3D DSM reconstruction than the sparse MAMI image sequence processing (b). We attribute this primarily to the accuracy of the sensor pose metadata available with the satellite image pair, but also to the more favorable overhead perspective provided by the satellite.

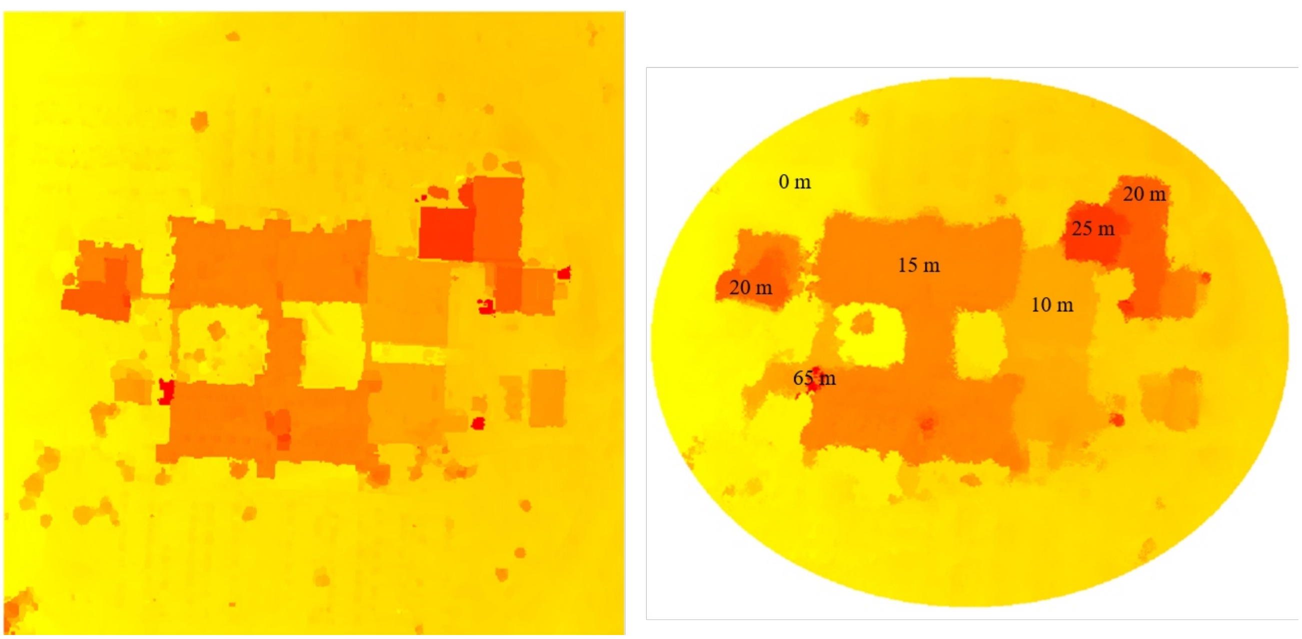

Figure 6. Reconstructed 3D digital surface models of the ROI.

2.3 Compressed Sensing SAR Reconstruction

We begin by modifying Equation 2 to incorporate a sparsity prior:

$$\hat{a} = \underset{a}{\operatorname{argmin}} \underbrace{\|y_{\text{measured}} - \mathcal{F}(\bar{K}, \bar{X}) \cdot a\|_2}_{data-consistency} + \underbrace{\lambda\|\psi a\|_1}_{sparsity} \tag{3}$$

where ψ represents a sparsifying transform, such as a 3D wavelet transform. The essence of this approach is to estimate $\hat{a}$ that not only satisfies the data-consistency term with respect to the radar measurements, but finds the *sparsest* image by minimizing its ℓ_1 norm after transform ψ, which results in modest performance improvements.

The Fourier operator $\mathcal{F}$ can be implemented via a (differentiable) matrix multiply, but for improved performance we utilize the NUFFT Type-I provided by the `sigpy` package, and for convenience defined its gradient with respect to the parameters a by its adjoint (NUFFT Type-II operation),[14–16] which can be combined with standard `PyTorch` autograd optimizer routines such as `SGD` or `Adam`. Figure 7 provides an numerical example on the selected ROI, demonstrating improved performance over the least-squares method. Note that the image visualization at higher iterations is limited by the dynamic range of the image.

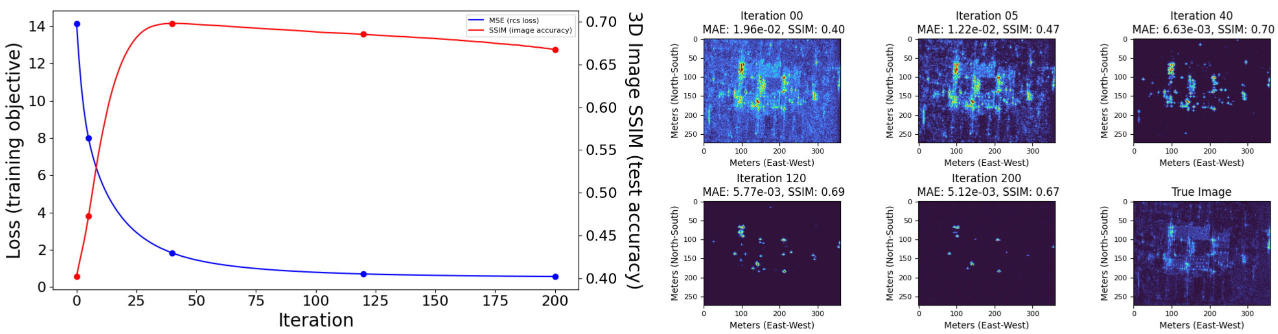

Figure 7. Optimization of the data-consistency mean-square error (MSE) and ℓ_1-wavelet sparsity terms using the Adam optimizer (initial learning rate 0.01). Unlike the least-squares case, here the SSIM is considerably improved over the initial backprojected image for several iterations achieving a best SSIM of 0.70 around iteration 38 with respect to the assumed groundtruth 3D SAR image. However, similar to the least-squares case, the SSIM eventually plateaus and decreases with additional descent on the objective, resulting in point-like structures at later iterations that do not correlate well with the target-scene, indicating that the sparsity objective is not sufficient by itself for achieving robust 3D SAR imaging.

2.4 Joint-Sparsity Priors

The issue with the previous approach for airborne SAR is that it places a large emphasis on finding a sparse solution with very few measurements, which themselves are not geometrically diverse. When a radar platform observes a target-scene from a single aspect angle there is inherent ambiguity in the 3D reconstruction, which often manifests as streaking or range ambiguity in 3D visualizations. This repetition can often be summarized using a sparse set of coefficients, which implies that conventional sparse reconstruction with limited aspect angle diversity yields solutions that are *overly* sparse and not representative of the true 3D sparsity structure.

Instead, joint-sparsity priors can help guide the optimization process by encouraging the resulting 3D image to *match* the sparsity level or pattern of a reference or prior image.[17] While some approaches have utilized subsets of the radar data itself,[18] here we propose utilizing a *multi-modal* prior derived from EO imagery. In particular, leveraging 3D EO reconstruction algorithms described in Section 2.2.4, we generate a 3D EO point-cloud that can be geographically aligned with the SAR data and combined via the joint sparsity objective:

$$\hat{a} = \underset{a}{\operatorname{argmin}} \underbrace{\|y_{\text{measured}} - \mathcal{F}(\bar{K}, \bar{X}) \cdot a\|_2}_{data-consistency} + \underbrace{\lambda\|[\psi a, \psi z_{\text{prior}}]^T\|_{2,1}}_{joint-sparsity} \tag{4}$$

where z_{prior} represents an image-domain prior or reference image that is used to guide the SAR reconstruction. The essence of this approach is to relax the sparsity constraints on the image a to instead match the sparsity pattern of a higher-resolution EO image, while ensuring the data-consistency check as before. While the EO image or 3D model may be historical, and not provide up-to-date information captured by the SAR data colect, the sparsity pattern of the EO prior is likely to be similar to the sparsity pattern of the SAR image since they are both representing 3D structure of scatterers in the target-scene.

Figure 7 provides an numerical example on the selected ROI, demonstrating improved performance over the least-squares and $\ell 1$-wavelet sparsity methods. Note that the image visualization at higher iterations is limited by the dynamic range of the image. Note here that the 3D EO model was generated from imagery collected *after* the GOTCHA SAR data collect, and includes buildings not present in the SAR data (depicted in Figure 3b).

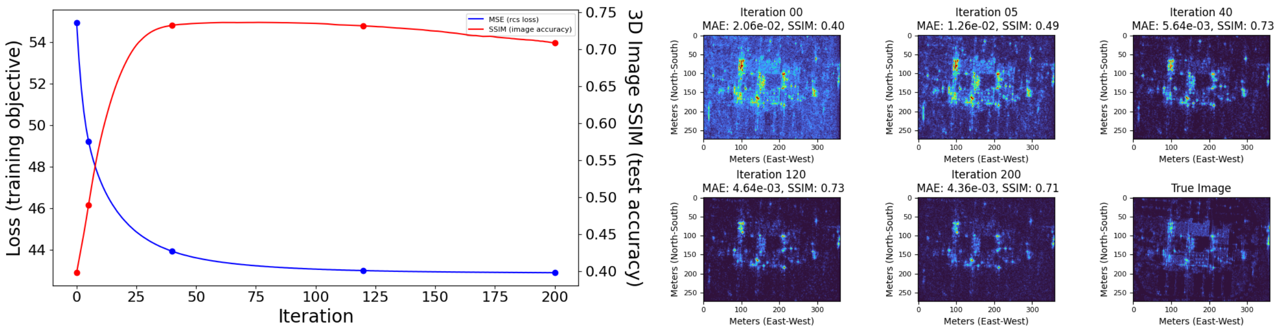

Figure 8. Optimization of the data-consistency mean-square error (MSE) and $\ell_{2,1}$-wavelet joint-sparsity terms using the Adam optimizer (initial learning rate 0.01). Utilizing the EO prior (BETTER 3D model) improves the performance of ℓ_1-sparsity vase, yielding a best SSIM of 0.76 around iteration 53 with respect to the assumed groundtruth 3D SAR image. However, due to the autograd-based gradient descent formulation, once the joint-sparsity objetive term is close in value to the MSE loss, the MSE loss may start to dominate, which results a plateau and decrease in the SSIM value after the peak. This scenario may be avoided by implementing a better proximal gradient operator for the minimization problem.

2.5 Performance Metrics

We define a few different performance metrics to evaluate the performance of 3D SAR reconstructions:

- *Image-domain 3D mean-absolute error (MAE)*: We define this metric using the true SAR image x_{true} that is assumed to be the groundtruth, and the SAR image estimate $x_{\text{estimated}}$) produced by each method, as:

$$\text{MAE}(x_{\text{true}}, \hat{x}_{\text{estimated}}) = \frac{1}{\|x_{\text{true}}\|} \|x_{\text{true}} - \hat{x}_{\text{estimated}}\|_1 \tag{5}$$

- *Image-domain 3D structural similarity index measure (SSIM)*: We define this metric using the true SAR image ($x = x_t exttrue$) that is assumed to be the groundtruth, and the SAR image estimate ($y = x_{\text{estimated}}$)) produced by each method, as:

$$\text{SSIM}(x, y) = \frac{(2\mu_x\mu_y + c_1)(2\sigma_{xy} + c_2)}{(\mu_x^2 + \mu_y^2 + c_1)(\sigma_x^2 + \sigma_y^2 + c_2)} \tag{6}$$

  where μ_x and σ_x^2 represent the mean and variance of volume $x_t exttrue$, μ_y and σ_y^2 represent the mean and variance of volume $x_{\text{estimated}}$), σ_{xy} represents the covariance of $x_t exttrue$ and $x_{\text{estimated}}$), and c_* is chosen proportional to the dynamic range of pixel values.[19]

- *Digital Surface Model (DSM) Height Error*: We define this metric using a separately collected LiDAR groundtruth DSM z_{LIDAR} and the estimated height-map resolved from the SAR reconstruction $\hat{z}_{\text{estimated}}$ by taking the argmax of the maximum intensity projection on the z (height) axis, as:

$$\text{MAE}(z_{\text{lidar}}, \hat{z}_{\text{estimated}}) = \frac{1}{\|z_{\text{lidar}}\|} \sum \|z_{\text{true}} - \hat{z}_{\text{estimated}}\|_1 \tag{7}$$

3. RESULTS

Figure 2 depicts the performance of the least-squares iterative reconstruction. Figure 7 depicts the performance of the ℓ_1-wavelet compressed sensing iterative reconstruction. Figure 8 depicts the performance of the $\ell_{2,1}$-wavelet joint-sparsity compressed sensing iterative reconstruction. For each of these experiments, we pick the image achieving the optimal reconstruction quality, defined here as the highest 3D SSIM with respect to the groundtruth SAR image. The resulting 3D reconstructed height maps are depicted in Figure 9 below. The resulting 3D reconstruction metrics are summarized in Table 1 below.

Algorithm	3D MAE	3D SSIM	DSM Error
Backprojection	1.964×10^{-2}	0.402	6.70 m
Least-Squares	9.789×10^{-3}	0.535	7.04 m
ℓ_1-Wavelet Sparsity	6.604×10^{-3}	0.701	6.61 m
$\ell_{2,1}$ EO-SAR Joint-Sparsity (BETTER)	$\mathbf{4.918 \times 10^{-3}}$	**0.757**	**5.56 m**

Table 1. Summary of metrics associated with the best 3D SAR images formed using different reconstruction algorithms.

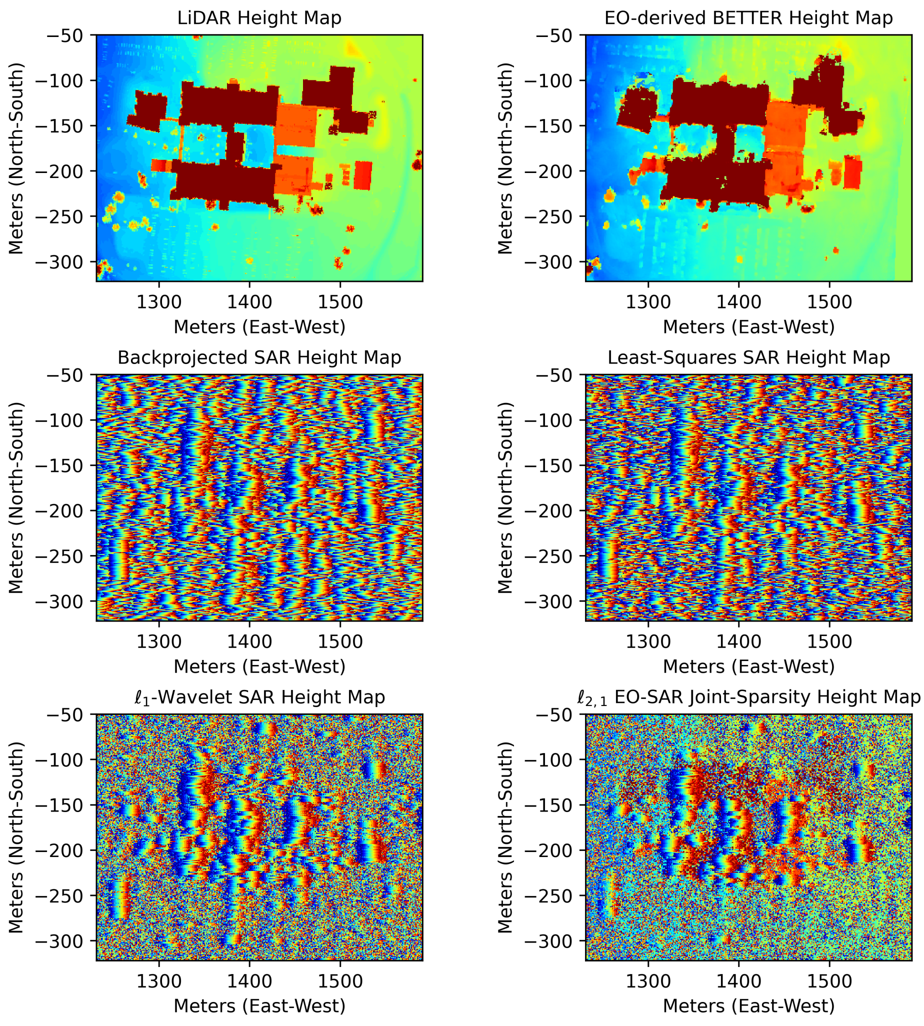

Figure 9. 3D height maps resulting from various reconstruction methods. The regularized reconstructions provide a considerable improvement in 3D height estimation. Each plot is plotted on the same color axis extending from 0 m altitude (blue) to 22 m altitude (red).

4. DISCUSSION

Our results (Table 1) numerically demonstrate the improvements in 3D MSE, 3D SSIM, and altitude estimation using the proposed EO-SAR joint-sparsity compressed sensing reconstruction algorithm, offering modest improvements over all methods compared. The height maps depicted in Figure 9 demonstrate how the joint-sparsity objective improves on 3D depth estimation, with the outline of all building edges starting to emerge. Both the ℓ_1-wavelet sparsity algorithm and $\ell_{2,1}$-wavelet EO-SAR joint-sparsity sparsity algorithm provide considerable improvements in the 3D structure estimation compared to backprojection and least-squares, which we attribute to 3D image prior that crucially is applied here in the sparsifying wavelet transform domain.

Note that the LiDAR and BETTER 3D models include a building in the top right corner of the the ROI that does not appear in the SAR data (Figure 3), likely due to construction after the AFRL GOTCHA SAR collect. This building does *not* appear in the final joint-sparsity SAR image, despite incorporating the BETTER 3D EO model as a prior since the algorithm ensures satisfaction of the radar data-consistency term. This is an important feature of the joint-sparsity approach, since it *does not require concurrent EO-SAR imaging*, although the best performance can be a achieved with more accurate 3D priors.

This is desirable in airborne applications because it is unlikely that an aperture with sufficient diversity would be subtended to enable both 3D EO model and a 3D SAR model generation concurrently on the same platform. The joint-sparsity approach excels in this setting since it does not enforce that both modalities (EO and SAR) match in the content of the target-scene, but only that their structure in the transform domain are similar.[5] This enables strong data consistency not provided by conventional image-fusion techniques.

However, one issue with the existing implementation of this technique is that it relies on gradient descent of the joint regularized objective, which not only requires an appropriate choice of λ (chosen heuristically here as 0.001) but also challenges the ability to find the *sparsest* solution while maintaining an appropriate level of error in the data-consistency term. Once an appropriate level is determined via empirical testing, a better solution would be to descend on the objective using high-performance convex optimization algorithms, such as the Fast Iterative Shrinkage Threshold Algorithm (FISTA)[20] or those provided via CVX[21] .

Finally, even with regularized reconstructions, there will likely remain ambiguity in the 3D SAR image. One approach for addressing this is via incorporation of additional SAR aspects, as in multi-look SAR.[22] However, one issue here is in the aspect-dependent radar cross section for common objects, such as trihedrals, metallic plates, and wires. Future work in this area may consider additional data-driven improvements for filtering or refining the resulting 3D SAR image to reveal the underlying structure of the target-scene such as via point-clouds.

5. CONCLUSION

We introduced a technique for incorporating 3D EO priors into 3D SAR image reconstruction algorithms via a $\ell_{2,1}$ joint-sparsity EO-SAR wavelet regularization term that guides the sparsity pattern of the estimated SAR image. The historical EO model priors are generated using Toyon's state of the art airborne and satellite 3D EO model reconstruction algorithms. The current implementation balances radar data-consistency terms with the regularization via choice of hyperparameter λ, but this approach can be improved by utilizing high-performance convex optimization algorithms that allow a specified tolerance on the radar data. The approach demonstrates improvements in 3D reconstruction performance both in image similarity and error and in 3D terrain height estimation on the AFRL GOTCHA data with respect to a groundtruth LiDAR digital surface model.

ACKNOWLEDGMENTS

This work was supported by Air Force grant #FA8650-22-C-1010, DARPA grant #HR001122S0016-22-3667, and NIH/NIBIB grant #F32EB030411.

REFERENCES

[1] Narayanan, R. M., Wood, N. S., and Lewis, B. P., "Assessment of Various Multimodal Fusion Approaches Using Synthetic Aperture Radar (SAR) and Electro-Optical (EO) Imagery for Vehicle Classification via Neural Networks," *Sensors* **23**(4), 2207 (2023).

[2] Rajagopal, A., Stier, N., Nelson, W., Chandrasekaran, S., and Brown, A. P., "DeepOSM-3D: recognition in aerial LiDAR RGBD imagery," in [*Geospatial informatics X*], **11398**, 67–84, SPIE (2020).

[3] Fontana, A., Berens, P., Staglianò, D., and Martorella, M., "3D ISAR/SAR imaging using multichannel real data," in [*2016 IEEE Radar Conference (RadarConf)*], 1–4, IEEE (2016).

[4] Li, Z., Zhang, X., Yang, Q., Xiao, Y., An, H., Yang, H., Wu, J., and Yang, J., "Hybrid SAR-ISAR image formation via joint FrFT-WVD processing for BFSAR ship target high-resolution imaging," *IEEE Transactions on Geoscience and Remote Sensing* **60**, 1–13 (2021).

[5] Rajagopal, A., Dwork, N., Hope, T. A., and Larson, P. E., "Enhanced PET/MRI reconstruction via dichromatic interpolation of domain-translated zero-dose PET," in [*Medical Imaging 2021: Physics of Medical Imaging*], **11595**, 1127–1135, SPIE (2021).

[6] Waxman, A., Aguilar, M., Baxter, R., Fay, D., and Ireland, D., "Opponent-color fusion of multi-sensor imagery: visible, IR and SAR," tech. rep., Massachusetts, Institute of Technology, Lincoln Lab, Lexington, MA (1998).

[7] Aksu, R., Rahman, M. M., and Gurbuz, S. Z., "3D scene reconstruction from multi-sensor EO-SAR data," in [*Algorithms for Synthetic Aperture Radar Imagery XXVII*], **11393**, 47–52, SPIE (2020).

[8] Barron, J. T., Mildenhall, B., Tancik, M., Hedman, P., Martin-Brualla, R., and Srinivasan, P. P., "Mip-nerf: A multiscale representation for anti-aliasing neural radiance fields," in [*Proceedings of the IEEE/CVF International Conference on Computer Vision*], 5855–5864 (2021).

[9] Fridovich-Keil, S., Yu, A., Tancik, M., Chen, Q., Recht, B., and Kanazawa, A., "Plenoxels: Radiance fields without neural networks," in [*Proceedings of the IEEE/CVF Conference on Computer Vision and Pattern Recognition*], 5501–5510 (2022).

[10] Liu, Z., Yang, S., Feng, Z., Gao, Q., and Wang, M., "Fast SAR autofocus based on ensemble convolutional extreme learning machine," *Remote Sensing* **13**(14), 2683 (2021).

[11] Scarborough, S. M., Gorham, L., Minardi, M. J., Majumder, U. K., Judge, M. G., Moore, L., Novak, L., Jaroszewksi, S., Spoldi, L., and Pieramico, A., "A challenge problem for SAR change detection and data compression," in [*Algorithms for Synthetic Aperture Radar Imagery XVII*], **7699**, 287–291, SPIE (2010).

[12] Barnett, A. H., Magland, J., and af Klinteberg, L., "A parallel nonuniform fast Fourier transform library based on an "Exponential of semicircl" kernel," *SIAM Journal on Scientific Computing* **41**(5), C479–C504 (2019).

[13] Dungan, K. E., Gorham, L. A., and Moore, L. J., "SAR digital spotlight implementation in MATLAB," in [*Algorithms for Synthetic Aperture Radar Imagery XX*], **8746**, 80–90, SPIE (2013).

[14] Fessler, J. A. and Sutton, B. P., "Nonuniform fast Fourier transforms using min-max interpolation," *IEEE transactions on signal processing* **51**(2), 560–574 (2003).

[15] Beatty, P. J., Nishimura, D. G., and Pauly, J. M., "Rapid gridding reconstruction with a minimal oversampling ratio," *IEEE transactions on medical imaging* **24**(6), 799–808 (2005).

[16] Ong, F. and Lustig, M., "SigPy: a python package for high performance iterative reconstruction," in [*Proceedings of the ISMRM 27th Annual Meeting, Montreal, Quebec, Canada*], **4819**, 5 (2019).

[17] Gelb, A. and Scarnati, T., "Reducing effects of bad data using variance based joint sparsity recovery," *Journal of Scientific Computing* **78**(1), 94–120 (2019).

[18] Zhang, J., Gelb, A., and Scarnati, T., "Empirical Bayesian Inference Using a Support Informed Prior," *SIAM/ASA Journal on Uncertainty Quantification* **10**(2), 745–774 (2022).

[19] Wang, Z., Simoncelli, E. P., and Bovik, A. C., "Multiscale structural similarity for image quality assessment," in [*The Thrity-Seventh Asilomar Conference on Signals, Systems & Computers, 2003*], **2**, 1398–1402, Ieee (2003).

[20] Kim, D. and Fessler, J. A., "Another look at the fast iterative shrinkage/thresholding algorithm (FISTA)," *SIAM Journal on Optimization* **28**(1), 223–250 (2018).

[21] Diamond, S. and Boyd, S., "CVXPY: A Python-embedded modeling language for convex optimization," *The Journal of Machine Learning Research* **17**(1), 2909–2913 (2016).

[22] Dungan, K. E. and Potter, L. C., "3-D imaging of vehicles using wide aperture radar," *IEEE Transactions on Aerospace and Electronic Systems* **47**(1), 187–200 (2011).